Wiley Analytical Science

Wiley Analytical Science Virtual Conference

November 9-17

For the 3rd time, The Wiley Analytical Science Conference is back!

It's all happening November 9 - 17

The Wiley Analytical Science Virtual Conference will bring together thousands of researchers and practitioners to share current developments in science and industry. Join for exciting presentations from experts in the fields of analytical and bioanalytical chemistry, pharmaceutical research, materials science, lab automation, and related disciplines.

Register to learn about recent developments & applications in:

- Microscopy
- Spectroscopy
- Mass Spectrometry
- Separation Science
- Much more!

Register here

WILEY

ADVANCED ENERGY MATERIALS
www.advenergymat.de

Interaction between Water Wave and Geometrical Structures of Floating Triboelectric Nanogenerators

Shuxing Xu, Guanlin Liu, Jinbiao Wang, Honggui Wen, Sheng Cao, Huilu Yao, Lingyu Wan,* and Zhong Lin Wang**

Although triboelectric nanogenerators (TENGs) are highly efficient and adaptable in harvesting ocean wave energy, the dynamics of floating TENGs in underwater wave stimulations have so far rarely been studied. Herein, the interactions between centimeter-scaled floating structures and water waves are experimentally revealed. By integrating inertial measurement units into the shells of various floating TENG structures, the primary acceleration data associated with different parameters are obtained. Based on the data of 63 literature reported floating TENGs, a series of experimental parameters are elaborately probed, including shell shape, shell size, weight, barycenter, wave strength/frequency, and wave-producing methods. Through dynamic calculations, each can offer the kernel data of acceleration and frequency distribution curves, revealing several regularities in water–structure interactions associated with TENGs. These calculations could serve as guidance for the design of the future floating TENGs in blue energy harvesting.

1. Introduction

Found on the principles of triboelectricity and electrostatic induction,[1–3] the emerging triboelectric nanogenerator (TENG)[4,5] technology provides an effective method for harvesting high-entropy vibration,[6,7] wind energy,[8,9] water wave energy,[10,11] and other types of mechanical energy[12,13] in the environment. Because TENGs possess high conversion efficiency of energy and can be fabricated with simple processes at low cost out of abundant raw materials,[14] the use of TENGs to harvest random and low-frequency energy has gained a great deal of interest in the research area of energy harvesting, especially in harvesting widely distributed water wave energy.[15–18] Because of these advantages, a wide variety of TENGs have been proposed, and many achievements have been made. A TENG is capable of delivering instantaneous power density over 10 MW m^{-2} at a low frequency of ≈1 Hz;[19] a hybrid pendulum-type blue energy harvester can harvest all-weather ocean wave energy;[20] a water buoyancy multifrequency water wave energy generator is able to output a voltage of 1221 V and a current of 147 μA.[21] Despite all those achievements have been made, most previous studies only focus on the design and optimization of various structures for water wave energy collection,[22,23] while the kinematics of TENGs floating on water waves have seldom been studied, as to our knowledge. Only if the interactive relationship between the floating TENGs and water wave has been understood, the TENGs based on it could have higher sensitivity and conversion efficiency in moving water.

Reviewing existing studies on floating TENGs is beneficial to our study of wave–structure interaction and determination of the experimental parameters. Prior to experiments, we collect 63 excellent papers with high quality, high impact factors (IF > 10 at 2021) among a large number of floating TENGs from October 2013 to January 2021. As **Figure 1** shows, TENG shapes can be divided into four categories: sphere, box, cylinder, and other. Each type can be further divided according to more specific parameters. Apparently, spherical shells[24] are the most widely used, followed by cubic shapes[25] and cylindrical shapes.[26] In addition to these regularly designed geometric shapes, other shapes have also been used in the design of floating TENG, including imitations,[27] bionics,[28] gear,[29] and other geometric shapes,[30,31] which demonstrates the wide variety of floating TENGs. Each number on the outer ring in Figure 1 corresponds to a citation of a reviewed paper shown in Table S1 in the Supporting Information which shows the shape, size, thumbnail, and wave-producing method of a floating TENG. Those would be referred in the following experiments. Although floating TENGs vary in shape, researchers have rarely dig how to set the parameters of the floating structure or how to design floating TENGs to improve the water wave energy absorption coefficients. In many cases, floating TENGs would have to rely on some lightweight foams to raise the waterline and maintain balance so as to improve the response to water waves.[26,32,33] All of these may lead to asynchronization between water waves and floating TENGs, thereby wasting

S. Xu, G. Liu, J. Wang, H. Wen, S. Cao, H. Yao, L. Wan, Z. L. Wang
Center on Nanoenergy Research
School of Physical Science & Technology
Guangxi University
Nanning 530004, P. R. China
E-mail: guanlinliu@gxu.edu.cn; lyw2017@gxu.edu.cn; zhong.wang@mse.gatech.edu
S. Xu, Z. L. Wang
Beijing Institute of Nanoenergy and Nanosystems
Chinese Academy of Sciences
Beijing 101400, P. R. China

The ORCID identification number(s) for the author(s) of this article can be found under https://doi.org/10.1002/aenm.202103408.

DOI: 10.1002/aenm.202103408

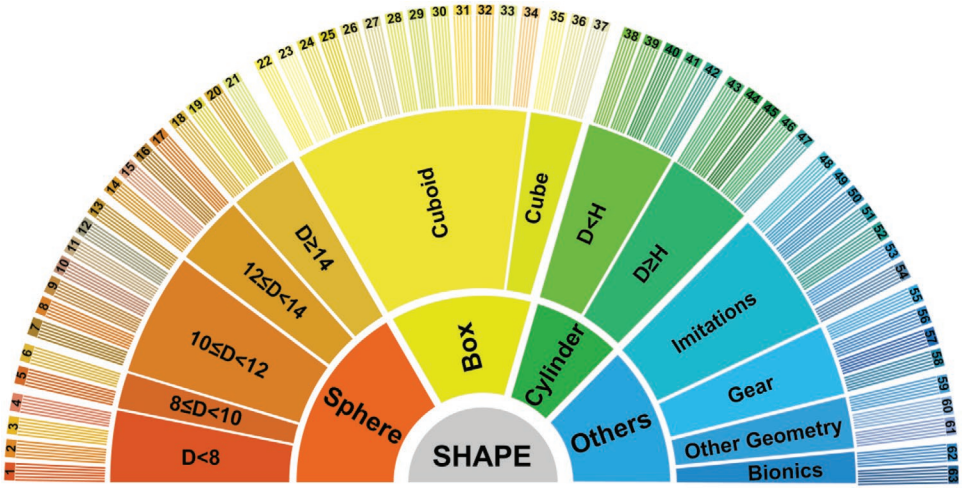

Figure 1. Various shapes of floating TENGs. Sixty-three papers related to floating TENGs are categorized by their outer shell and furthermore specific parameters, based on which the following experiments could have more serviceability and good pertinence.

the hard-won and fleeting blue energy. Therefore, a study on the wave-structure interaction of floating TENGs is particularly important.

In this study, we explore the kinematic relationship between water waves and centimeter-scaled floating structures by embedding inertial measurement units (IMUs) into the shells of different floating structures, which are specially made to capture the kinetic data in different conditions real timely, thus to find out the interaction characteristics through the later dynamic analysis. Based on the literature review of previous floating TENGs, we elaborately conduct a series of experiments to obtain the acceleration data of the IMU-embedded floating structures by changing various kernel parameters such as shell shape, shell size, weight, height of the barycenter, wave strength/frequency, and wave-making method. We perform dynamic analysis on the acquired data, including bias removal, filtering, sampling, statistic distribution calculation, curve fitting, and kernel data selection, from which we draw the frequency distribution graphs and average acceleration graphs. Based on these graphs, we reveal several rules of wave-structure interaction, including the behavior of the same float under different water wave conditions, and the effects of the same water wave on floats with different structural parameters. In addition, we acquire data from a real scenario in the Beibu Gulf to investigate the diversity between ocean waves and artificial waves. These quantitative test results can effectively aid the future floating TENG layout and optimization to improve output efficiency in water wave energy harvesting, and also provide a guide toward standardization and practicality.

2. Results and Discussion

In order to experimentally simulate real water waves with high enough energy, and to resist water wave suppression resulting from reaction by the floats,[34] we used a large-capacity wave-producing tank, which was 1.2 m long, 1 m wide, 1 m deep, and has a water depth of 60 cm, and twenty high-power wave-producing pumps (50 W each) to generate large waves that were not prone to disturbance (Figure S1, Supporting Information). Through a master switch, all the water wave-producing pumps worked in the same phase, frequency, and power during the experiments so that regular and controllable water waves were obtained. In order to ensure float operation accuracy and motion data stability, we used IMUs from BEWIS SENSING, model BW-IMU500C, which had high accuracy, excellent zero-bias stability, small size, low weight, and resolution of up to 10^{-4} m s^{-2} (as detailed in Figures S2 and S3 and Note S1, Supporting Information), to acquire motion accelerations a_x, a_y, and a_z that can reflect the forces exerted upon the floating structures along the three axes. Once an IMU was forced to move, its acceleration curve fluctuated around the zero tick mark, as shown in **Figure 2**a (wherein the curve has been debiased and filtered, and the unit g = 9.8 m s^{-2} is the earth's gravitational acceleration). In all the experiments, an IMU was mounted horizontally to the geometric center of the floating structure with a 3D-printed polylactic acid (PLA) bracket. An example of a spherical floating structure is shown in Figure 2b and Figures S4 and S5 (Supporting Information). The ring-shaped mass in the lower part was used to adjust the waterline and the barycenter. The details and fabrication process can be found in the experiment sections and Note S2 (Supporting Information).

The most common waves are wind-generated waves, which are disordered in time and space. The wave energy is affected by many factors, such as wind, gravity, Earth's deflecting force, earthquakes, planetary motion, and surface tension.[35] Although waves are complex and change constantly, they show a clear periodic characteristic. Mathematically, ocean waves can be regarded as being composed of multiple simple harmonics with different strengths, frequencies, and phases.[36] The wave-front equation at a point can be written as:

$$H(t) = \sum_{n=1}^{\infty} \mathrm{H}_n = \sum_{n=1}^{\infty} \mathrm{a}_n \cos(\omega_n \mathrm{t} + \varepsilon_n) \tag{1}$$

where H is the height of the wave surface above the static water surface, a is the amplitude of the component wave, ω is the angular frequency of the component wave, t is the time, and

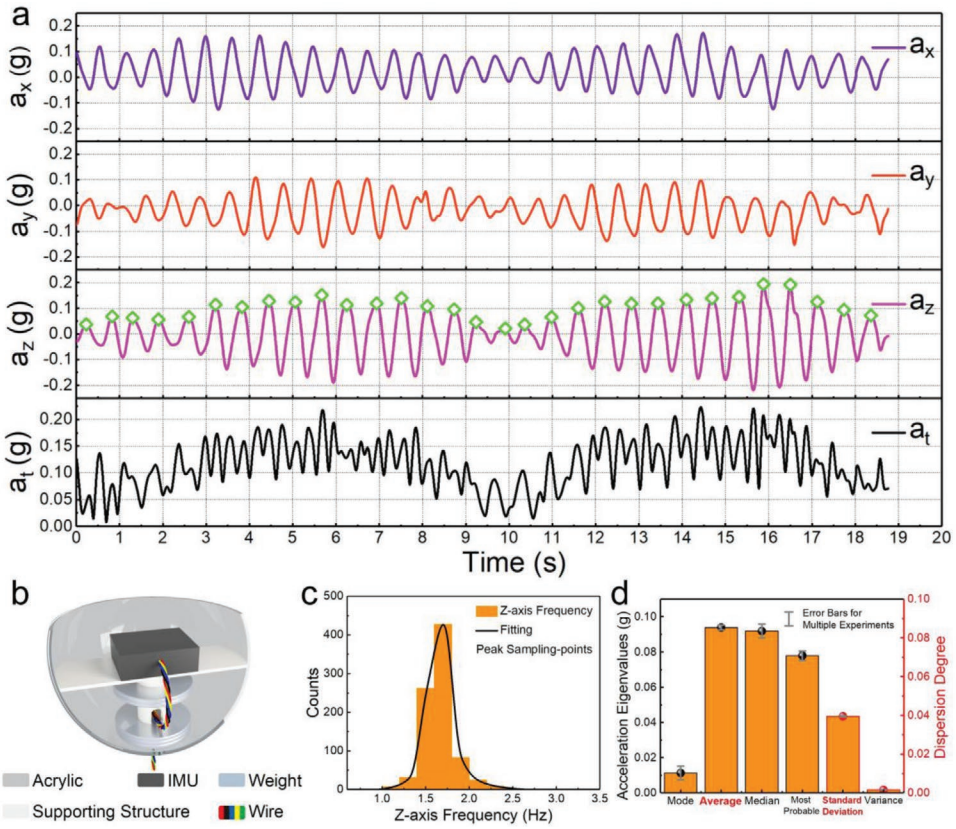

Figure 2. Principle and configuration of the test. & Output characteristic of device and data analysis. a) The details of three axial acceleration curves (a_x, a_y and a_z) and the total acceleration (a_t) calculated from them. The green marks on the *z*-axis acceleration curve are the positions of the wave crests sought by programming algorithm. The time difference of adjacent marks is the motion period of the float, becomes motion frequency after reciprocal, and is counted in graph c. b) Schematic of the spherical float setup. c) Frequency distribution histogram of *z*-axis acceleration and its fitted distribution curve with 20 min of the test time. The frequency distribution histogram is the count statistics of the motion frequency falling in each interval. d) The eigenvalues and dispersion degree extracted from total acceleration under multiple experiments, where the error bar is the standard deviation of these experiments. The frequency distribution curve in graph c and the kernel data bolded in graph d are selected for comparison in the following figures.

ε is the phase factor corresponding to NO. n component wave. Mathematically, the acceleration equation of the wave surface can be obtained from the second derivative of the above wave surface displacement equation. The wave surface acceleration equation also follows the principle of simple harmonic superposition, which is also reflected in the three-axis acceleration curves obtained by the laboratory wave simulation shown in Figure 2a. In all our experiments, the acceleration data of the three axes were collected by the IMU at 115 200 baud rate for 20 min. After data preprocessing, the total acceleration a_t was calculated using the following equation: $a_t = \sqrt{a_x^2 + a_y^2 + a_z^2}$. The resulting a_x, a_y, a_z and a_t were then substituted into a series of kinetic calculations, described below, to obtain the data and curves reflecting the motion of the floating structure.

The data preprocessing included debiasing and filtering. The orientation of the IMU was not completely horizontal, so debiasing was performed in order to improve the accuracy of subsequent calculation results. The debiasing was conducted by subtracting the arithmetic average of all the data of an axis from the acceleration data of the axis to achieve the acceleration curve fluctuating around the zero scale line (Note S3, Supporting Information). In addition, although the IMU output data passed through the sensor's Kalman filter,[37] some defects and clutter still existed in the output waveform, which could have affected the search process for peaks and troughs in the later stages. Hence, we used the moving average filtering on the debiased data. In this method, a new data point is constructed by averaging a data point and the following n data points (typically n = 20 in this study), and then the same process is conducted for the rest of the data points until the end of the data set (Note S4 and Figure S6, Supporting Information).

After the initial data preprocessing, we performed specific dynamic calculations to obtain the underlined dynamics of the floating structure represented by the data. The calculation process included data point sampling, distribution statistics analysis, frequency distribution curves fitting, and kernel acceleration data extraction. First of all, the purpose of data point sampling was to search for the positions of the peaks or troughs on an axial acceleration curve (the marks in Figure 2a and Figure S7, Supporting Information). From the results, the time differences of adjacent peaks or troughs, which represent the various motion cycles of the floating structure, were calculated, and its

reciprocal is the frequency. By counting the frequencies falling in frequency intervals, we obtained the frequency distribution histogram shown in Figure 2c. With interpolation fitting (Note S5 and Figure S8, Supporting Information), we obtained a curve in Figure 2c representing the motion frequency distribution of the floating structure. This type of curve reflects the floating structure motion frequency distribution in a certain period of time under preset specific conditions, and it serves as an important basis for the comparison of subsequent experimental results. Therefore, we used only the wave peaks for the subsequent analysis since sampling the peaks points or trough points were almost the same (Figure S9 and Note S6, Supporting Information). Furthermore, we emphasize the frequency distribution in the *z*-axis, because the water waves produced in the laboratory exhibit obvious periodicity in the vertical direction, and show relative randomness in the horizontal direction. From a curve of total acceleration, we extracted the average, most probable value, median, mode, standard deviation, and variance of acceleration that can characterize the forces exerted on the floating structure in a certain perspective (Figure 2d). After extensive comparison of the data (Note S7, Supporting Information), we used the average of acceleration, which represents the overall tendency of the data, and the standard deviation of acceleration, which represents the degree of dispersion of the data, as additional important metrics for comparing the experimental results of the floating structure dynamics.

The strength and frequency of external water waves have a huge impact on the output of a floating TENG.[38] Many previous studies have investigated the output characteristics of a specific floating TENG under different amplitudes and frequencies of a linear motor, or explored the voltage, current, charge, and other parameters under different water wave conditions.[11,24,32] However, no study has ever quantitatively investigated the dynamic characteristics of floating structures for TENG. Here, the commonly used 12 cm spherical shell, shown in Figure 1, was selected to study the floating structure motion under different water wave strengths, frequencies, and wave-producing methods.

The 12 cm spherical floating structure was placed under four types of waves with successively increasing strengths ($S1 < S2 < S3 < S4$) and tested for 20 min. **Figure 3**a1 shows the frequency distribution curve of the test results along the *z*-axis (*x* and *y* axes in Figure S10, Supporting Information). The frequency distribution of the floating structure's upward motion in each axis is almost the same for the different water wave strengths. This invariant behavior is also observed in the three-axis average frequency shown in Figure S11 (Supporting Information). The average and standard deviation of acceleration of the floating structure increase significantly with wave strength (see Figure 3a2), which shows that the energy harvested by the floating structure increases with wave strength and is reflected in the average acceleration. In general, the wave strength has little effect on the motion frequency of the floating structure, and is positively correlated with the structure's motion intensity.

Similarly, we used four working frequencies ($F1 < F2 < F3 < F4$) of water wave-producing pumps to explore the effect of wave frequency on the motion frequency and the force exerted on the floating structure. Figure 3b1 shows the *z*-axis frequency distribution curves of a 12 cm spherical floating structure at four

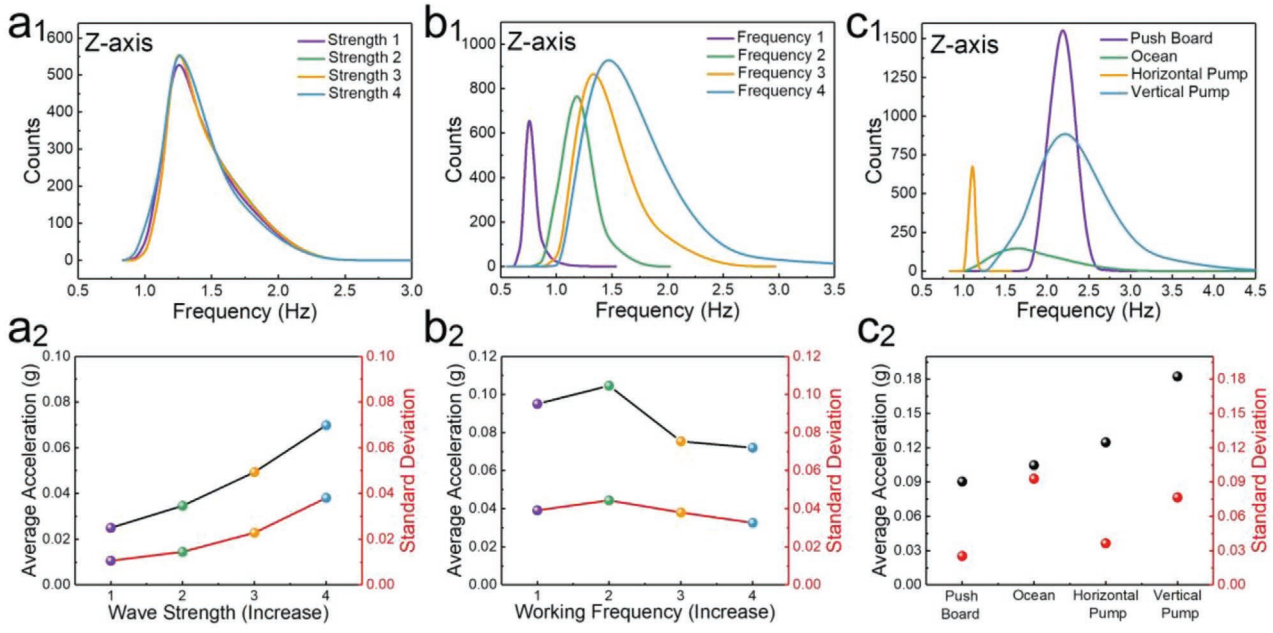

Figure 3. The effects of external water wave conditions on the motion of float. Frequency distribution curves and average acceleration under a1,a2) different wave strengths, b1,b2) different wave frequencies, and c1,c2) different wave-producing methods. The frequency distribution curves come from the frequency distribution histograms after fitted. And these histograms (similar to Figure 2c) are derived from counting the motion frequencies between adjacent peaks of the *z*-axis acceleration like those in Figure 2a. The test time of every experiment is all 20 min. The acceleration variation trend graphs contain the average of acceleration, which can represent the overall tendency of the data and reflects the force on floating structures from the side, while the standard deviations can show the degree of data dispersion.

wave-producing pump frequencies. Obviously, as the frequency of the wave-producing pumps increases, the *z*-axis frequency distribution curves shift toward higher frequencies, the value increase, and the curves broaden. This is because an increase in water wave frequency increases the number of cycles received by the floating structure within a time period. This eventually leads to an increase in the value of the frequency and a wider curve. As shown in Figure 3b2, the average and standard deviation of acceleration first increase and then decrease. Experimental observations have indicated that in actual situations, the increases of these values in the first stage are due to the direct conversion of the outputs of the wave-producing pumps into wave energy, and the floating structure moves more violently. However, with the further increase of the wave-producing pump frequency, the recoiled water waves affect the newly created waves, breaking the water surface and attenuating the water wave energy. This may lead to a decrease in the average and standard deviation of the total acceleration. The same behavior of first increasing and then decreasing also appears in the *x*- and *y*-axis frequency distribution and average frequency curves (Figures S12 and S13, Supporting Information).

The wave-producing method is an important factor affecting the output of floating TENGs. Based on the statistics in Table S1 (Supporting Information), we used four commonly used water wave types for investigation and testing: actual ocean waves,[14,32] waves generated by push-board,[21,38] waves generated by horizontal wave-producing pumps[26,28] or by vertical wave-producing pumps.[39] The ocean field test was carried out around 12 pm on January 12, 2021, in a site located at the east longitude of ≈109.53° and the north latitude of ≈21.30°, which is about 30 nautical miles from the shore of Tieshan Port in the Beibu Gulf. The air temperature was about 20 °C. The average wind speed was about 1.2 m s^{-1}. Like in the previous experiments, spherical structures with a diameter of 12 cm (Figure S14 and Note S8, Supporting Information) were used in the field test. All the other three tests were carried out in a special-made long water tank in the laboratory, where different forms of simulated water waves were generated with a strictly controlled water volume in the water tank, working frequency of the water-making apparatus, and many other factors (Figure S15 and Note S9, Supporting Information). The frequency distribution data generated by the four different wave-making methods are shown in Figure 3c1 and Figures S16 and S17 (Supporting Information). The peaks of the *z*-axis frequency curves increase in the order of ocean waves, horizontal pump waves, vertical pump waves, and push-board waves. The most probable frequencies of the curves increase in the order of horizontal pump waves, ocean waves, push-board waves, and vertical pump waves. In particular, because the wind and water waves were relatively small at the time of the ocean field test, the frequencies of the water waves were low (Video S1, Supporting Information), which led its peak and the most probable frequency to be relatively small. Frequency distribution broadening increases in the order of horizontal pump waves, push-board waves, ocean waves, and vertical pump waves. This observation indicates the randomness of ocean waves, and that the frequency range of ocean waves is greater than the frequency ranges of water waves generated in the laboratory. In addition, it can be seen from the figure that the frequency distributions associated with the horizontal and vertical wave-producing pumps are much different, with the former being narrowly distributed in the low-frequency range, and the latter being the opposite. Waves generated by different wave-producing methods exert different forces on the floating structure. It can be seen from Figure 3c2 that the average accelerations of pumps waves are significantly higher than those of ocean waves and the push-board waves. This indicates that the forces of the ocean water waves on the floating structure in the field test are lower than the forces of the water waves generated by the wave-producing pumps on the floating structure. The average acceleration results from the vertical pump waves are the highest, which is why this wave-making method has been used in many studies in order to obtain higher electricity outputs.[11,39,40] The standard deviation of acceleration in the ocean field test is significantly greater than that associated with the other wave-producing methods, indicating that ocean water wave acceleration is more dispersive and more random. This property is determined by the time-domain characteristics and frequency-domain characteristics of ocean waves. These observations indicate that it is necessary to use multiple frequencies to drive device tests under laboratory conditions.[41]

In addition to external water wave environments, the parameters of the floating structures such as shape, size, weight, and barycenter also have important impacts on the output of the floating TENGs. In this section, we explore the effects of the above variables on the motion of floating structures through a controlled variables approach.

TENGs that harvest water wave energy have a variety of shapes.[42] We chose regular geometric shapes: sphere, short cylinder (S-cylinder), tall cylinder (T-cylinder), cuboid, and cube, shown in Figure 1, as the shapes to study. We fabricated the five kinds of shells with the same volume of 904.7 cm^3 (equivalent to a sphere with a diameter of 12 cm) and with their barycenter located at one-third of their height (Figures S18 and S19, Supporting Information). While keeping the water wave strength and frequency constant during the experiments (Video S2, Supporting Information), we tested the wave–structure interaction data of those shells, and obtained the corresponding frequency distribution curves (**Figure 4**a1, Figure S20, Supporting Information) and acceleration kernel data graphs (Figure 4a2). The *z*-axis frequency distribution graphs show that the central tendencies of the curves are roughly the same, and the most probable frequencies are also almost the same. It can be seen that the shape of the floating structure has little effect on the *z*-axis response frequency. However, some shells have double peaks on their *x*-axis and *y*-axis frequency distribution curves (Figure S20, Supporting Information). This may be due to the horizontal rotations of the floating shells during the experiments. Figure 4a2 depicts that the average and standard deviation of acceleration for the cube are both the largest. The order of the average and standard deviation of acceleration from highest to lowest is cube, tall cylinder, cuboid, short cylinder, and sphere. Compared with the smooth spherical shell, the cubic shell with edges and corners is more easily coupled with water waves, and it receives greater force and harvests more water wave energy. Given the difference between the cube and the sphere, 2D two-phase flow fluid–solid coupling simulations of water-sphere interaction and water-cube interaction were

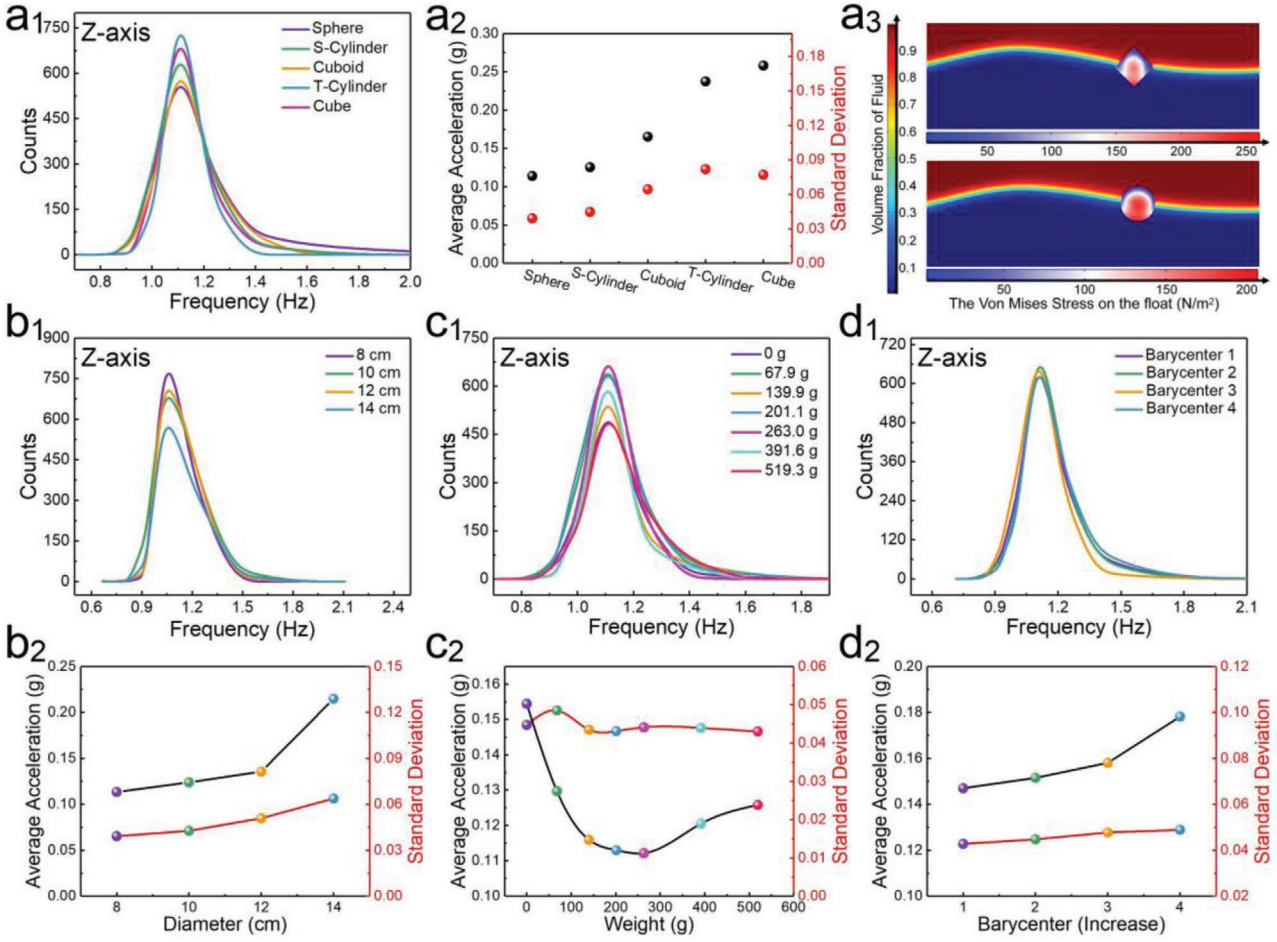

Figure 4. The effects of internal structural parameters on the motion of float. a1) Frequency distribution curves and a2) average acceleration of floating structures with different shapes. a3) COMSOL simulation of cubical and spherical float under the same water wave situation. In this graph, the horizontal scale is the Von Mises Stress on the float (unit is N m^{-2}) and the vertical scale is the volume fraction of the fluid (1 represents water, 0 represents air). Frequency distribution curve and the average acceleration of floats with b1,b2) different sizes, c1,c2) different weights, and d1,d2) different centers of gravity.

performed (Figure 4a3 and Note S10 and Video S3, Supporting Information) using COMSOL software. In this picture, the color on the float is the Von Mises Stress it receives (as shown on the abscissa) and the color of the fluid is its volume fraction (as shown on the ordinate). Under the same volume fraction (1 represents water, 0 represents air), we compared the Von Mises Stress (unit N m^{-2}) of the two floating structures under the same wave action. The results show that the force on the cube is indeed greater than that on the sphere, verifying that the cube in the above experiment has more advantages in wave-structure interaction from the numerical simulation.

We also conducted experiments on the different diameters of spherical shells to explore the interaction between water waves and floating TENGs of different sizes.[43] Based on the review data shown in Figure 1, spherical shells with diameters of 8, 10, 12, and 14 cm were chosen. The barycenter of each fabricated spherical structure (Figures S21 and S22, Supporting Information) was set to one third of the vertical diameter. Under the same wave conditions, we obtained the frequency distribution curves (Figure 4b1 for the *z* axis, Figure S23, Supporting Information, for the *x* and *y* axes), and the trends of the average and the standard deviation of acceleration (Figure 4b2). The most probable frequency basically does not change with the increase of diameter, indicating that the *z*-axis response frequency of the floating spheric shell basically does not change with the size. The information in Figure 4b2 clearly illuminates that the average and standard deviation of acceleration increase monotonously with the diameter. The larger the area that interacts with the waves, and the greater the impact force received from water waves. This is why the average and standard deviation of acceleration increase with the diameter as shown in Figure 4b2. This also inspired us to adopt a larger size shell to help improve TENG absorption of water wave energy.

The different weights of floating structures directly affect their draughts and responses to acceleration at the same force. For investigation, we applied different weights (0 g, 67.9 g, 139 g, 201 g, 263 g, 396 g, and 519 g) to a spherical floating structure with a diameter of 12 cm (Figure S24, Supporting Information) and strictly controlled the barycenter to maintain it at one third of the diameter (4 cm) from the bottom. It can be seen from Figure 4c1 that the most probable frequencies do not change with the weight, indicating that the change

of the weight almost does not affect the response frequency of the *z*-axis of the structure (*x*, *y* axes and the combination in Figure S25, Supporting Information). Figure 4c2 depicts that as the weight increases, the average total acceleration possesses a trend of first decreasing and then slowly increasing, and the standard deviation of acceleration fluctuates slightly. For the draught situation (Figure S26, Supporting Information), the average acceleration drops significantly when the waterline over the middle draught. As the weight continues to increase from the middle draught, the average acceleration rises slightly. This trend results from the combined effect of complex factors, such as changes in buoyancy under the action of water waves and weight. In general, for a spherical floating structure, a high draught or heavy mass is not conducive to wave energy harvesting, especially when the draught is located near the middle of a spherical shell.

In the above experiments, the barycenter of each floating structure is located at one third of the diameter. However, a change in the barycenter may have an impact on the interaction between the floating structure and waves. Thus, by adjusting the position of the internal weight ring in the vertical direction (Figures S27 and S28, Supporting Information) while keeping other parameters unchanged, we sequentially increased the position of the barycenter ($B1 < B2 < B3 < B4$) of four floating sphere structures with a 12 cm diameter (see Note S11, Supporting Information for the calculation of the barycenter). Then we investigated the effect of the barycenter on the motion of the floating spheres under the same external wave conditions. The experimental results are demonstrated in Figure 4d1–2 and Figure S29 (Supporting Information) with the frequency distribution curves and average acceleration scatter plots. The heights of the z-axis response frequency curves output by the spheres with different centers of gravity are highly coincident, indicating that the position of the barycenter has little effect on frequency. As can be seen from Figure 4d2, as the barycenter moves upward, the average and standard deviation of acceleration both show an upward trend. This may be due to the fact that as the barycenter approaches the sphere center, under the same force of water waves, the rotational torque of the floating sphere becomes smaller and thus the conversion into rotational energy becomes smaller. As a result, the kinetic energy of translation is increased, which is manifested by an increase of average acceleration. This also suggests that the barycenter of a sphere being close to the center of the sphere is beneficial to improving the conversion efficiency for translational kinetic energy.

There are several shortcomings in this study, such as considering a floating TENG as a rigid body, insufficient data associated with damping from the ocean field test, and using the local coordinate system of the floating structure instead of the inertial coordinate system. In spite of these shortcomings, the results of this study have revealed a number of empirical trends under many complex interference factors and are expected to inspire further research and investigation.

3. Conclusion

In this paper, leveraging the findings of 63 previous studies, we designed and conducted experimental investigations on the interaction between water wave and geometrical structures of floating triboelectric nanogenerators. By embedding the measuring inertial instruments into different floating shells, and putting the elaborated floats into the matching test environment, the original accelerated velocity under various parameters is received. Using the specific dynamic analysis to calculate the obtained raw data, the frequency distribution and the eigenvalue of acceleration can be obtained. By comparing the frequency distribution curves and the kernel data of total acceleration, we revealed several regularities from our investigation as follows.

The wave absorption capacity of a cubic shell is the highest due to its sharp edges and nonstreamlined surface. The wave response capacity of a spherical shell is positively related to the wave strength, the diameter of the shell, and the height of the barycenter, and it exhibits a trend of first decreasing and then slightly increasing with the increase of weight. Compared with other wave-producing methods, the vertical wave-producing pumps can provide waves that lead to stronger floating structure motion. The fluctuation and response frequency of ocean waves observed in the field test is wider than those observed in the laboratory conditions. As for other response frequencies of a floating structure is only related to the water wave frequency and has nothing to do with its own parameters. These trends can guide the future design of wave energy TENGs and the improvement of laboratory conditions, and more importantly, assist researchers to take much more attention to the structural design for high efficiency.

4. Experimental Section

Shell Fabrication: The four types of spherical shells (with 8, 10, 12, and 14 cm diameters) used in the experiment were formed by splicing and sealing two overedged hemispherical shells with the same diameter. A hole with a radius of 3 mm was made at the bottom of each spherical shell. The overedges for the 8 and 10 cm hemispheres are 6 mm, and 4 holes are made on the edge. Those of 12 and 14 cm hemispheres were 8 mm and 6 holes. The diameter of all holes on the overedges is 3 mm. The cuboids, cubes, and cylinders were drawn using 3dmax drawing software and were 3D printed with a shell thickness of 3 mm using R4600 epoxy resin as the material. Detailed information can be found in Supporting Information as the main text indexes.

Assembly and Packaging: T-shaped support structures were made of PLA (Figure S5a, Supporting Information) and printed by a 3D printer (model CREALITY, CR-2020). The hollow shells of different shapes and sizes each had their respective supporting structures. For example, the supporting structure in a spherical shell with a diameter of 12 cm weighed only 17 g. An IMU was mounted on the center of the supporting structure, and its wires ran to the outside through the hollow T-shaped support structures. Then a counterweight (standard galvanized gaskets) was affixed with a small amount of glue on the support structure at the predefined location to ensure that the overall barycenter of the structure was in the preset position. Except for the experiment exploring the change of the barycenter, the barycenter of each floating structure was fixed at a height of one-third of the shell's diameter or height. The fabricated internal parts were assembled into the corresponding shells, the wires were fed through the hole under each shell, and finally the entire internal structure was fixed with a small amount of glue. A custom-made silicone sealing ring was added to the middle of each spherical shell for waterproofing. Then the two hemispherical shells and the sealing ring were tightly fixed with screws. Finally, the feedthroughs in the middle and at the bottom of the shell were sealed with silica gel (Kafuter 706).

Measurements: The large-scale wave pool used for the measurement is custom-made, with an external size of 120 cm × 100 cm × 100 cm and a fixed water depth of 60 cm. The size of the standard water tank used to explore different wave-producing methods was 160 cm × 40 cm × 40 cm and the water depth was 18 cm. The wave-producing pump model was Jiebao RW20. The IMU sensor model was BW-IMU500C. The sampling period of the experiment was 100 Hz, and the data were collected at 115 200 baud rate. All the test times were 20 min. At least three groups were measured in each experiment. The lengths of all the wires extended into the wave-producing tank were about 90 cm. The water wave strength and frequency were kept constant, except in the experiment involving different wave environments.

Supporting Information

Supporting Information is available from the Wiley Online Library or from the author.

Acknowledgements

The research was supported by National Natural Science Foundation of China (81560300) and Guangxi Natural Science Foundation project (2020JJA160133).

Conflict of Interest

The authors declare no conflict of interest.

Author Contributions

S.X. and G.L. conceived the project and designed the experiment part. S.X. and J.W. reviewed papers about floating TENGs. S.X. and H.W. fabricated the devices and completed the tests. H.Y. and L.W. helped build the experimental setup. S.X., G.L., S.C., and L.W. wrote the manuscript. G.L. and Z.L.W. supervised the project.

Data Availability Statement

The data that support the findings of this study are available from the corresponding author upon reasonable request.

Keywords

float, triboelectric nanogenerators, water waves, wave–structure interactions

Received: November 2, 2021
Revised: November 28, 2021
Published online:

[1] S. W. Niu, L. Lin, Y. Liu, Y. S. Zhou, Y. Hua, Z. L. Wang, *Energy Environ. Sci.* **2013**, *6*, 3576.
[2] C. Xu, B. Zhang, A. C. Wang, H. Zou, G. Liu, W. Ding, C. Wu, M. Ma, P. Feng, Z. Lin, Z. L. Wang, *ACS Nano* **2019**, *13*, 2034.
[3] H. T. Baytekin, B. Baytekin, S. Soh, B. A. Grzybowski, *Angew. Chem.* **2011**, *50*, 6766.
[4] F. R. Fan, Z. Q. Tian, Z. L. Wang, *Nano Energy* **2012**, *1*, 328.
[5] Z. L. Wang, *ACS Nano* **2013**, *7*, 9533.
[6] G. Liu, J. Chen, Q. Tang, L. Feng, H. Yang, J. Li, Y. Xi, X. Wang, C. Hu, *Adv. Energy Mater.* **2018**, *8*, 1703086.
[7] H. Guo, X. Pu, J. Chen, Y. Meng, M. H. Yeh, G. Liu, Q. Tang, B. Chen, D. Liu, S. Qi, C. Wu, C. Hu, J. Wang, Z. L. Wang, *Sci. Rob.* **2018**, *3*, 2516.
[8] J. Bae, J. Lee, S. Kim, J. Ha, B. S. Lee, Y. Park, C. Choong, J. B. Kim, Z. L. Wang, H. Y. Kim, J. J. Park, U. I. Chung, *Nat. Commun.* **2014**, *5*, 4929.
[9] L. Zhang, B. Zhang, J. Chen, L. Jin, W. Deng, J. Tang, H. Zhang, H. Pan, M. Zhu, W. Yang, Z. L. Wang, *Adv. Mater.* **2016**, *28*, 1650.
[10] G. Liu, L. Xiao, C. Chen, W. Liu, X. Pu, Z. Wu, C. Hu, Z. L. Wang, *Nano Energy* **2020**, *75*, 104975.
[11] X. Liang, T. Jiang, G. Liu, Y. Feng, C. Zhang, Z. L. Wang, *Energy Environ. Sci.* **2020**, *13*, 277.
[12] C. Li, D. Liu, C. Xu, Z. Wang, S. Shu, Z. Sun, W. Tang, Z. L. Wang, *Nat. Commun.* **2021**, *12*, 2950.
[13] Y. Liu, N. Sun, J. Liu, Z. Wen, X. Sun, S. T. Lee, B. Sun, *ACS Nano* **2018**, *12*, 2893.
[14] Z. Zhou, X. Li, Y. Wu, H. Zhang, Z. Lin, K. Meng, Z. Lin, Q. He, C. Sun, J. Yang, Z. L. Wang, *Nano Energy* **2018**, *53*, 501.
[15] S. Chu, A. Majumdar, *Nature* **2012**, *488*, 294.
[16] J. Tollefson, *Nature* **2014**, *508*, 302.
[17] C. Zhang, L. Liu, L. Zhou, X. Yin, X. Wei, Y. Hu, Y. Liu, S. Chen, J. Wang, Z. L. Wang, *ACS Nano* **2020**, *14*, 7092.
[18] N. Li, L. Qiao, J. He, S. Wang, L. Yu, P. Murto, X. Li, X. Xu, *Adv. Funct. Mater.* **2021**, *31*, 2008681.
[19] H. Wu, S. Wang, Z. Wang, Y. Zi, *Nat. Commun.* **2021**, *12*, 5470.
[20] L. Liu, Q. Shi, C. Lee, *Nano Energy* **2020**, *76*, 105052.
[21] K. Xia, J. Fu, Z. Xu, *Adv. Energy Mater.* **2020**, *10*, 2000426.
[22] H. Chen, C. Xing, Y. Lia, J. Wang, Y. Xu, *Sustainable Energy Fuels* **2020**, *4*, 1063.
[23] Z. L. Wang, T. Jiang, L. Xu, *Nano Energy* **2017**, *39*, 9.
[24] Z. Lin, B. Zhang, H. Guo, Z. Wu, H. Zou, J. Yang, Z. L. Wang, *Nano Energy* **2019**, *64*, 103908.
[25] J. Chen, J. Yang, Z. Li, X. Fan, Y. Zi, Q. Jing, H. Guo, Z. Wen, K. C. Pradel, S. Niu, Z. L. Wang, *ACS Nano* **2015**, *9*, 3324.
[26] C. Hou, T. Chen, Y. Li, M. Huang, Q. Shi, H. Liu, L. Sun, C. Lee, *Nano Energy* **2019**, *63*, 103871.
[27] Z. Zhao, Z. Zhang, L. Xu, F. Gao, B. Zhao, Z. Kang, Q. Liao, Y. Zhang, *Nano Energy* **2020**, *76*, 104960.
[28] Z. S. Ahmed, I. Hassan, Y. Zi, Y. Xi, X. He, J. Zu, Z. L. Wang, *Adv. Energy Mater.* **2017**, *7*, 1601705.
[29] Y. Xi, H. Guo, Y. Zi, X. Li, J. Wang, J. Deng, S. Li, C. Hu, X. Cao, Z. L. Wang, *Adv. Energy Mater.* **2017**, *7*, 1602397.
[30] W. Liu, L. Xu, T. Bu, H. Yang, G. Liu, W. Li, Y. Pang, C. Hu, C. Zhang, T. Cheng, *Nano Energy* **2019**, *58*, 499.
[31] L. M. Zhang, C. B. Han, T. Jiang, T. Zhou, X. H. Li, C. Zhang, Z. L. Wang, *Nano Energy* **2016**, *22*, 87.
[32] L. Gao, S. Lu, W. Xie, X. Chen, L. Wu, T. Wang, A. Wang, C. Yue, D. Tong, W. Lei, H. Yu, X. He, X. Mu, Z. L. Wang, Y. Yang, *Nano Energy* **2020**, *72*, 104684.
[33] L. Feng, G. Liu, H. Guo, Q. Tang, X. Pu, J. Chen, X. Wang, Y. Xi, C. Hu, *Nano Energy* **2018**, *47*, 217.
[34] D. Zhang, J. Shi, Y. Si, T. Li, *Nano Energy* **2019**, *61*, 132.
[35] M. Onorato, S. Residori, U. Bortolozzo, A. Montina, F. T. Arecchi, *Phys. Rep.* **2013**, *528*, 47.
[36] P. Kumar, *Rev. Geophys.* **1997**, *35*, 385.
[37] R. E. Kalman, *J. Basic Eng.* **1960**, *82*, 35.
[38] J. An, Z. M. Wang, T. Jiang, X. Liang, Z. L. Wang, *Adv. Funct. Mater.* **2019**, *29*, 1904867.
[39] T. X. Xiao, X. Liang, T. Jiang, L. Xu, J. J. Shao, J. H. Nie, Y. Bai, W. Zhong, Z. L. Wang, *Adv. Funct. Mater.* **2018**, *28*, 1802634.
[40] L. Xu, T. Jiang, P. Lin, J. J. Shao, C. He, W. Zhong, X. Y. Chen, Z. L. Wang, *ACS Nano* **2018**, *12*, 1849.
[41] H. Pang, Y. Feng, J. An, P. Chen, J. Han, T. Jiang, Z. L. Wang, *Adv. Funct. Mater.* **2021**, *31*, 2106398.
[42] K. Zhang, Y. Wang, Y. Yang, *Adv. Funct. Mater.* **2019**, *29*, 1806435.
[43] Y. Pang, S. Chen, Y. Chu, Z. L. Wang, C. Cao, *Nano Energy* **2019**, *66*, 104131.